

## Control of $I$ - $V$ Hysteresis in $\text{CH}_3\text{NH}_3\text{PbI}_3$ Perovskite Solar Cell

Hui-Seon Kim,<sup>†</sup> In-Hyuk Jang,<sup>†</sup> Namyoun Ahn,<sup>‡</sup> Mansoo Choi,<sup>‡</sup> Antonio Guerrero,<sup>§</sup> Juan Bisquert,<sup>§,||</sup> and Nam-Gyu Park<sup>\*,†</sup>

<sup>†</sup>School of Chemical Engineering and Department of Energy Science, Sungkyunkwan University, Suwon 440-746, Korea

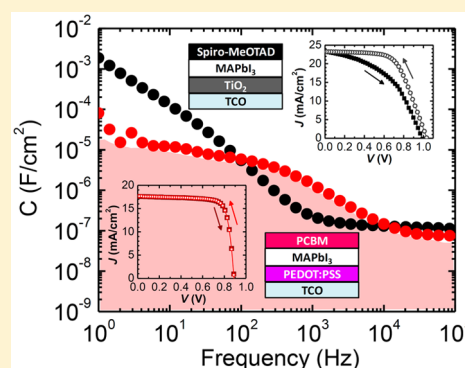
<sup>‡</sup>Department of Mechanical and Aerospace Engineering, Seoul National University, Seoul 151-742, Korea

<sup>§</sup>Institute of Advanced Materials (INAM), Universitat Jaume I, 12006 Castelló, Spain

<sup>||</sup>Department of Chemistry, Faculty of Science, King Abdulaziz University, Jeddah, Saudi Arabia

### S Supporting Information

**ABSTRACT:** Mismatch of current ( $I$ )-voltage ( $V$ ) curves with respect to the scan direction, so-called  $I$ - $V$  hysteresis, raises critical issue in  $\text{MAPbI}_3$  ( $\text{MA} = \text{CH}_3\text{NH}_3$ ) perovskite solar cell. Although ferroelectric and ion migration have been proposed as a basis for the hysteresis, origin of hysteresis has not been apparently unraveled. We report here on the origin of  $I$ - $V$  hysteresis of perovskite solar cell that was systematically evaluated by the interface-dependent electrode polarizations. Frequency ( $f$ )-dependent capacitance ( $C$ ) revealed that the normal planar structure with the  $\text{TiO}_2/\text{MAPbI}_3/\text{spiro-MeOTAD}$  configuration showed most significant  $I$ - $V$  hysteresis along with highest capacitance ( $10^{-2}$   $\text{F}/\text{cm}^2$ ) among the studied cell configurations. Substantial reduction in capacitance to  $10^{-3}$   $\text{F}/\text{cm}^2$  was observed upon replacing  $\text{TiO}_2$  with PCBM, indicative of the  $\text{TiO}_2$  layer being mainly responsible for the hysteresis. The capacitance was intensively reduced to  $10^{-5}$   $\text{F}/\text{cm}^2$  and  $C$ - $f$  feature shifted to higher frequency for the hysteresis-free planar structures with combination of PEDOT:PSS, NiO, and PCBM, which underlines the spiro-MeOTAD in part contributes to the hysteresis. This work is expected to provide a key to the solution of the problem on  $I$ - $V$  hysteresis in perovskite solar cell.



Since the report on 9.7% efficient solid-state perovskite solar cell in 2012<sup>1</sup> following the 3–6% perovskite-sensitized liquid junction solar cells reported in 2009<sup>2</sup> and 2011,<sup>3</sup> there has been a surge of researches on perovskite solar cell due to superb photovoltaic performance. As a result, power conversion efficiency (PCE) reached 20%.<sup>4,5</sup> In order to approach such a high PCE a variety of attempts have been made<sup>6–9</sup> based on fundamental understanding of organolead halide perovskite.<sup>10–13</sup> So far,  $\text{CH}_3\text{NH}_3\text{PbI}_3$  ( $\text{MAPbI}_3$ ) is the most well-established material because of reproducibly high PCE. Nevertheless, a considerable portion of unique phenomena of  $\text{MAPbI}_3$  perovskite solar cell, such as giant dielectric constant, ferroelectric behavior, switchable photovoltaics and  $I$ - $V$  hysteresis, has not been fully understood.<sup>14–20</sup> It was observed that the output current was significantly influenced by the time-dependent capacitive current, which eventually caused  $I$ - $V$  hysteresis.<sup>18–20</sup> In terms of solar cell operation, huge capacitive current can easily lead to overestimation or underestimation due to the difficulty of reaching steady-state, which prevents us from obtaining precise photovoltaic parameters at a given condition. Furthermore, unraveled origin of transient behavior impedes full utilization of  $\text{MAPbI}_3$  material and, thus, limits the possibility for application in other fields. From this aspect, origin of the slow kinetics has been extensively analyzed using various techniques, where switchable photovoltaic effect was reported based on the manipulated electric field by ion

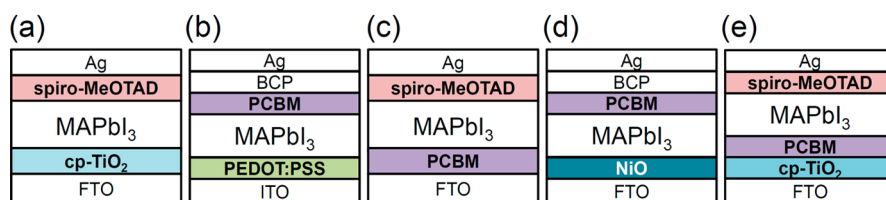
drift.<sup>17,21</sup> Theoretical calculations also supports the existence of ion defects in  $\text{MAPbI}_3$ ,<sup>22</sup> which is consistent with the experimental results showing density of state converted from frequency-dependent capacitance.<sup>23</sup> Therefore, the localized electric field is sufficiently built at the contacts owing to the ion redistribution by applying bias voltage,<sup>19,20,24</sup> which is mirrored by electrode polarization.<sup>25</sup> However, it is still uncertain how the electrode polarization is made at the interface of  $\text{MAPbI}_3$ , where the capacitive current is highly dependent on the selective contacts. For example, the inverted planar layout with poly(3,4-ethylenedioxythiophene) polystyrenesulfonate (PEDOT:PSS) and [6,6]-phenyl C61 butyric acid methyl ester (PCBM) is a typical hysteresis-free structure showing almost no capacitive current at room temperature.<sup>26,27</sup> From this point of view, we designed the diverse device configurations with various selective contacts to elucidate interface-dependent electrode polarization.

Figure 1 illustrates each device architecture used in this study, where  $\text{TiO}_2$  and PCBM are incorporated as an electron acceptor and a hole transport material is selected among 2,2',7,7'-tetrakis( $N,N$ -di-4-methoxyphenylamino)-9,9'-spirobifluorene (spiro-MeOTAD), PEDOT:PSS, and NiO. All

Received: October 12, 2015

Accepted: November 9, 2015

Published: November 9, 2015



**Figure 1.** Device architectures with different selective contact layers in planar structure. (a) Normal structure with compact TiO<sub>2</sub> (cp-TiO<sub>2</sub>)/MAPbI<sub>3</sub>/spiro-MeOTAD. (b) Inverted structure with PEDOT:PSS/MAPbI<sub>3</sub>/PCBM. (c) PCBM/MAPbI<sub>3</sub>/spiro-MeOTAD. (d) NiO/MAPbI<sub>3</sub>/PCBM. (e) cp-TiO<sub>2</sub>/PCBM/MAPbI<sub>3</sub>/spiro-MeOTAD.

architectures with various selective contacts are prepared with a planar type where MAPbI<sub>3</sub> perovskite layer is sandwiched between electron and hole selective contacts. The planar structure allows us to easily replace each selective electrode giving comparable contact area, which excludes the effect of charge flux varied with interface area.<sup>28,29</sup> We have studied the representative normal and inverted structures shown in Figure 1a and b, which was followed by investigating the remaining structures (Figure 1c–e) consisting of different combination of selective contacts to figure out the origin of *I*–*V* hysteresis.

*I*–*V* hysteresis of the normal structure (cp-TiO<sub>2</sub>/MAPbI<sub>3</sub>/spiro-MeOTAD, Figure 1a) and the inverted structure (PEDOT:PSS/MAPbI<sub>3</sub>/PCBM, Figure 1b) is shown in Figure 2a and b, respectively. The normal structure demonstrates

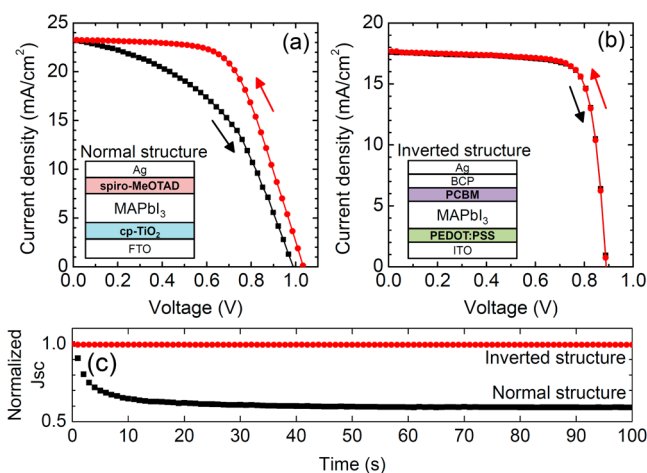


**Figure 2.** *I*–*V* hysteresis and time-dependent photocurrent. (a) Scan direction-dependent *I*–*V* curves of the cp-TiO<sub>2</sub>/MAPbI<sub>3</sub>/spiro-MeOTAD (normal) structure and (b) the PEDOT:PSS/MAPbI<sub>3</sub>/PCBM (inverted) structure. During *I*–*V* scan, the current was acquired 100 ms after applying a given voltage (voltage settling time = 100 ms). (c) Normalized time-dependent *J*<sub>sc</sub> of the normal and the inverted structures. Open-circuit condition under one sun illumination was maintained before measuring *J*<sub>sc</sub>.

severe *I*–*V* hysteresis (Figure 2a), whereas the inverted structure shows hysteresis-free characteristics (Figure 2b). Scan rate-dependent *I*–*V* characteristics are also investigated, which is shown in Supporting Information (SI) Figure S1 and S2. *I*–*V* hysteresis of the normal structure is dependent on the scan rate and becomes slightly alleviated with increasing voltage settling time (increasing scan rate), whereas the inverted structure shows constant *I*–*V* curve regardless of scan rate. The hysteresis tendency is in accordance with time-dependent photocurrent density (*J*<sub>sc</sub>) behavior as shown in Figure 2c. For the time-dependent *J*<sub>sc</sub> measurements, the devices were kept under one sun illumination (AM 1.5G, 100 mW/cm<sup>2</sup>) at open-

circuit condition, which was switched to short-circuit condition to measure *J*<sub>sc</sub> with time. In case of normal structure, *J*<sub>sc</sub> is exponentially decayed with time and reaches saturation point, which is attributed to the accumulated capacitive current.<sup>18</sup> No difference in *J*<sub>sc</sub> at short-circuit condition observed in Figure 2a in spite of huge capacitive current monitored in time-dependent *J*<sub>sc</sub> (Figure 2c) is due to the fact that a given voltage settling time (100 ms) is too short to distinguish the small difference in capacitive current. On the other hand, the inverted structure discharges negligible capacitive current leading to constant *J*<sub>sc</sub> regardless of light-soaking at the open-circuit condition, which indicates hysteresis-free behavior because *I*–*V* hysteresis results from voltage history-dependent capacitive current.

Frequency-dependent capacitance was obtained by using impedance spectroscopy. Capacitances measured at short-circuit condition without bias voltage in dark and under one sun illumination are shown in Figure 3a and b. Thanks to the

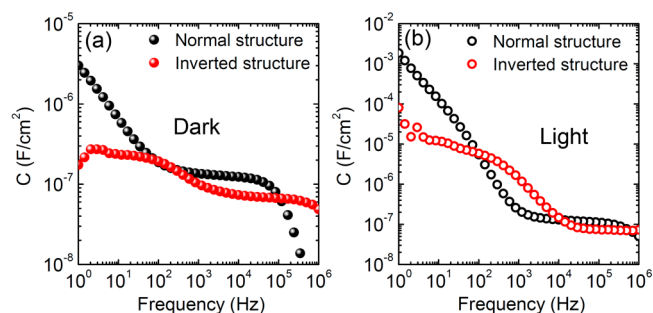


**Figure 3.** Frequency (*f*)-dependent capacitance (*C*). *C*–*f* curves (a) in dark and (b) under one sun illumination at short-circuit condition (bias voltage = 0 V). The normal and the inverted structures represent cp-TiO<sub>2</sub>/MAPbI<sub>3</sub>/spiro-MeOTAD and PEDOT:PSS/MAPbI<sub>3</sub>/PCBM, respectively.

recent intensive work on frequency-dependent capacitance of MAPbI<sub>3</sub>,<sup>25,30</sup> two capacitance steps observed in low and intermediate frequency have been well interpreted in terms of ionic and electronic behavior. The capacitance in intermediate frequency is due to electronic polarization in relation to dipole polarization or chemical capacitance in the perovskite, whereas the capacitance in low frequency was suggested as electrode polarization caused by interfacial phenomena such as electric or ionic charge accumulation at the interface of MAPbI<sub>3</sub>.<sup>19,20,24,25</sup> Typical capacitance by electrode polarization is in the range of 10<sup>-5</sup>–10<sup>-6</sup> F/cm<sup>2</sup>, which correlates to the chemically reactive sites at interface. Indeed, these values are observed from impedance measurement in dark condition. The inverted structure results in nearly 1 order of magnitude lower capacitance at low frequency (~1 Hz) than that of the normal structure in dark condition as can be seen in Figure 3a. The

only difference between normal and inverted structure is selective contacts as illustrated in Figure 1a and b. The significantly different capacitance values at low frequency, thus, is consequently attributed to the selective contact itself or its interface with MAPbI<sub>3</sub> layer, where much larger capacitance in the normal structure indicates that higher reactive sites may exist. It is worth noting that the capacitance inflection point, where the electrode polarization in low frequency is transformed to the dipole polarization in intermediate frequency, is highly dependent on the interface with selective contacts. A distinctive shift of inflection point is observed from 1 Hz for the normal structure to 300 Hz for the inverted structure, which indicates that the selective contact is capable of developing capacitance plateau faster by reducing chemical interactions between the selective contacts and ions in perovskite such as I<sup>-</sup> ion. In other words, it is speculated that the underlying chemical interaction between the selective contacts and iodide ions is likely to determine the electrode capacitance. The frequency-dependent capacitance is also investigated with increasing bias voltage (SI Figure S6). The specific *C*-*f* features of the normal and inverted structure are almost same regardless of bias voltage. Figure 3b shows frequency-dependent capacitances under illumination for the normal and the inverted structures. Capacitance of 10<sup>-2</sup> F/cm<sup>2</sup> is observed for the normal structure. These extremely high values cannot limit to merely the interface but might correlate to chemical reaction in the bulk of the selective contact layers such as TiO<sub>2</sub> or spiro-MeOTAD. Compared to the normal structure capacitance in the inverted configuration is significantly diminished to 10<sup>-5</sup> F/cm<sup>2</sup> that is related to interfacial electrode polarization. In addition, the inflection point shifts to higher frequency.

Because the reduced electrode polarization of the inverted structure is obtained by replacing both electron and hole selective contacts in the normal structure, it is required to investigate which interface has a major effect on the electrode polarization in low frequency range. We design diverse device structures with the combination of selective contacts, in which cp-TiO<sub>2</sub> or PCBM is used as an electron transport layer and spiro-MeOTAD, PEDOT:PSS, or NiO is selected as a hole transport layer. In the normal structure, cp-TiO<sub>2</sub> is replaced with PCBM but spiro-MeOTAD is not changed as shown in Figure 1c. Figure 4a shows *I*-*V* hysteresis obtained from the PCBM/MAPbI<sub>3</sub>/spiro-MeOTAD layout. Scan direction-dependent *I*-*V* hysteresis is greatly relieved compared to that of cp-TiO<sub>2</sub>/MAPbI<sub>3</sub>/spiro-MeOTAD structure.<sup>31-33</sup> Removal of *I*-*V* hysteresis at longer voltage settling time (500 ms) is observed for the PCBM/MAPbI<sub>3</sub>/spiro-MeOTAD structure as shown in SI Figure S3, which indicates that capacitive current is quickly dissipated or there is less capacitive current compared to cp-TiO<sub>2</sub> only. A similar structure is additionally made by simply inserting PCBM layer between cp-TiO<sub>2</sub> and MAPbI<sub>3</sub> layer (cp-TiO<sub>2</sub>/PCBM/MAPbI<sub>3</sub>/spiro-MeOTAD, Figure 1e), which shows comparable *I*-*V* hysteresis to that of PCBM/MAPbI<sub>3</sub>/spiro-MeOTAD structure when applying 100 ms of voltage settling time for current acquisition as shown in Figure 4b. It is noted from the scan rate-dependent *I*-*V* hysteresis that the hysteresis for the cp-TiO<sub>2</sub>/PCBM/MAPbI<sub>3</sub>/spiro-MeOTAD structure hardly disappears even at the longer voltage settling time (500 ms) (SI Figure S4) compared with that for the PCBM/MAPbI<sub>3</sub>/spiro-MeOTAD structure, which is ascribed to the presence of cp-TiO<sub>2</sub>. Lastly, the spiro-MeOTAD layer is replaced with NiO leaving PCBM layer as electron

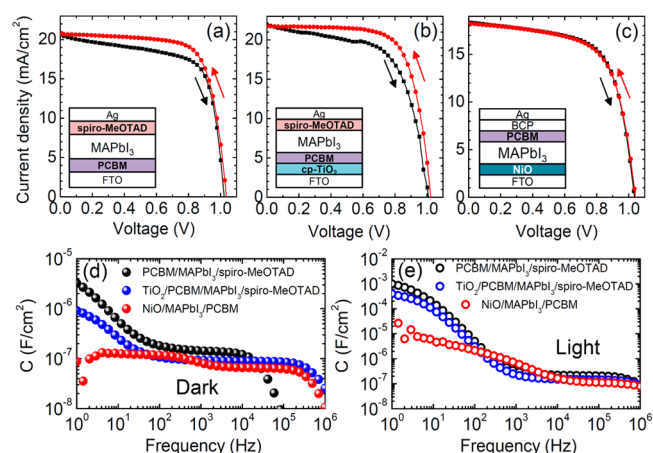


**Figure 4.** *I*-*V* hysteresis and *C*-*f* curves. Scan-direction-dependent *I*-*V* curves of (a) PCBM/MAPbI<sub>3</sub>/spiro-MeOTAD, (b) cp-TiO<sub>2</sub>/PCBM/MAPbI<sub>3</sub>/spiro-MeOTAD, and (c) NiO/MAPbI<sub>3</sub>/PCBM structures. Inset shows each device configuration. During *I*-*V* scan the current was acquired 100 ms after applying a given voltage. *C*-*f* curves measured (d) in dark and (e) under one sun illumination at short-circuit condition (bias voltage = 0 V).

transport layer as illustrated in Figure 1d. Interestingly, the NiO/MAPbI<sub>3</sub>/PCBM structure results in no *I*-*V* hysteresis as shown in Figure 4c. Scan rate-dependent *I*-*V* hysteresis is also measured (SI Figure S5) and no *I*-*V* hysteresis is confirmed. To closely correlate the *I*-*V* hysteresis phenomena with capacitance characteristics, impedance spectroscopy measurements are carried out. Figure 4d and e show frequency-dependent capacitance in dark and under illumination, respectively. When cp-TiO<sub>2</sub> layer is replaced with PCBM (PCBM/MAPbI<sub>3</sub>/spiro-MeOTAD), the capacitance at low frequency in dark and illumination is slightly lowered than the normal structure (cp-TiO<sub>2</sub>/MAPbI<sub>3</sub>/spiro-MeOTAD). In the case of cp-TiO<sub>2</sub>/PCBM/MAPbI<sub>3</sub>/spiro-MeOTAD structure, both capacitance values in dark and under illumination are considerably lowered compared to the normal structure, which is consistent with *I*-*V* hysteresis behavior. Therefore, the interface of MAPbI<sub>3</sub> with cp-TiO<sub>2</sub> is likely to contribute to significantly *I*-*V* hysteresis. Nevertheless, the remained interface of MAPbI<sub>3</sub> with spiro-MeOTAD also has a considerable effect on *I*-*V* hysteresis showing substantial increase in capacitance without complete development of plateau (electrode polarization) as frequency is lowered to 1 Hz (black and blue circles in Figure 4d). On the other hand, the capacitance at low frequency range found in PCBM/MAPbI<sub>3</sub>/spiro-MeOTAD structure (black circles in Figure 4d) or cp-TiO<sub>2</sub>/PCBM/MAPbI<sub>3</sub>/spiro-MeOTAD structure (blue circles in Figure 4d) is certainly reduced to 10<sup>-7</sup> F/cm<sup>2</sup> showing plateau when spiro-MeOTAD is simply replaced with NiO (red circles in Figure 4d). These low values indicate that the cell configurations containing PCBM and NiO are indicative of pure electrode polarization restricted to the interface. Under illumination a similar tendency is observed but capacitances are increased by 2 or 3 orders of magnitude. The distinctive difference in *C*-*f* feature among cp-TiO<sub>2</sub>/PCBM/MAPbI<sub>3</sub>/spiro-MeOTAD, PCBM/MAPbI<sub>3</sub>/spiro-MeOTAD, and NiO/MAPbI<sub>3</sub>/PCBM verifies that the MAPbI<sub>3</sub>/spiro-MeOTAD has a concrete effect on high capacitance as shown in Figure 4e. Therefore, we conclude that the interface of TiO<sub>2</sub>/MAPbI<sub>3</sub> has a dominant impact on the observed capacitive response at low frequencies, which is responsible for the slow transient behavior. Even in the

absence of the TiO<sub>2</sub>/MAPbI<sub>3</sub> interface, however, the *I*–*V* hysteresis is still observed due to the MAPbI<sub>3</sub>/spiro-MeOTAD interface, which probably suggests that chemical interactions are inferior to those observed for TiO<sub>2</sub>/MAPbI<sub>3</sub>. Although the perovskite layers in all devices with different substrates were fabricated by the exactly same process parameters, the morphology of perovskite films might be different. The formation and grain growth of perovskites could be sensitive to the selective contact layers, which may affect *I*–*V* hysteresis. Therefore, MAPbI<sub>3</sub> morphology was investigated (SI Figure S7). Morphology of MAPbI<sub>3</sub> grown on PEDOT:PSS (Figure S7a) is quite different from that grown on NiO (Figure S7b). However, both structures exhibit no *I*–*V* hysteresis, which underlines that the selective contacts rather than MAPbI<sub>3</sub> morphology plays more critical role in the hysteresis. In the case of PCBM-incorporated structures, morphology of MAPbI<sub>3</sub> grown on PCBM (Figure S7c) is similar to that grown on cp-TiO<sub>2</sub>/PCBM (Figure S7d), probably due to the same PCBM substrate. However, the extent of *I*–*V* hysteresis is different (SI Figure S3 and S4), which is again indicative of little dependence of *I*–*V* hysteresis on morphology.

To investigate interface dependent-capacitance quantitatively, the measured impedance spectra were fit with a simplified equivalent circuit. Table 1 shows the quantitative

**Table 1. Capacitance at Low Frequency,  $C_{LF}$ , and Inflection Frequency Depending on the Device Configurations**

structure	condition	$C_{LF}$ (F/cm <sup>2</sup> )	inflection frequency <sup>a</sup>
cp-TiO <sub>2</sub> /MAPbI <sub>3</sub> /spiro-MeOTAD	dark	$5.83 \times 10^{-6}$	$1 \times 10^0$ Hz
	light	$1.52 \times 10^{-2}$	$1 \times 10^0$ Hz
cp-TiO <sub>2</sub> /PCBM/MAPbI <sub>3</sub> /spiro-MeOTAD	dark	$1.21 \times 10^{-6}$	$2 \times 10^0$ Hz
	light	$6.67 \times 10^{-4}$	$1 \times 10^0$ Hz
PCBM/MAPbI <sub>3</sub> /spiro-MeOTAD	dark	$5.29 \times 10^{-6}$	$1 \times 10^0$ Hz
	light	$3.28 \times 10^{-3}$	$3 \times 10^0$ Hz
PEDOT:PSS/MAPbI <sub>3</sub> /PCBM	dark	$2.90 \times 10^{-7}$	$3 \times 10^2$ Hz
	light	$1.07 \times 10^{-5}$	$3 \times 10^2$ Hz
NiO/MAPbI <sub>3</sub> /PCBM	dark	$3.83 \times 10^{-7}$	$6 \times 10^2$ Hz
	light	$3.59 \times 10^{-6}$	<sup>b</sup>

<sup>a</sup>Inflection frequency was obtained from derivative of the *C*–*f* curve ( $-f \, dC/df$  vs *f* plot). <sup>b</sup>Ambiguous inflection point was observed.

capacitance values depending on the selective contacts. In the case of structures incorporating both cp-TiO<sub>2</sub> and spiro-MeOTAD layers, the capacitance reaches  $5.83 \times 10^{-6}$  F/cm<sup>2</sup>, which is decreased to  $1.21 \times 10^{-6} \sim 5.29 \times 10^{-6}$  F/cm<sup>2</sup> by eliminating the cp-TiO<sub>2</sub>/MAPbI<sub>3</sub> interface. Finally, the structures without both cp-TiO<sub>2</sub> and spiro-MeOTAD layers demonstrate much lower capacitance value of  $2.90 \times 10^{-7}$  and  $3.83 \times 10^{-7}$  F/cm<sup>2</sup> for PEDOT:PSS/MAPbI<sub>3</sub>/PCBM and NiO/MAPbI<sub>3</sub>/PCBM, respectively. The capacitance becomes intensified by about 3 orders of magnitude under illumination especially for the normal structure and the cp-TiO<sub>2</sub>/PCBM/MAPbI<sub>3</sub>/spiro-MeOTAD one. The device with both TiO<sub>2</sub> and spiro-MeOTAD results in the highest capacitance ranging  $\sim 10^{-2}$  F/cm<sup>2</sup> and the insertion of PCBM in between TiO<sub>2</sub> and MAPbI<sub>3</sub> exhibits slightly lower capacitance of  $\sim 10^{-3}$  F/cm<sup>2</sup>. Alternatively, devices without TiO<sub>2</sub> and spiro-MeOTAD generate significantly low capacitance of  $\sim 10^{-5}$  F/cm<sup>2</sup>. Inflection frequencies depending on the device configurations

are also described in Table 1. The inflection point obtained from the derivative of the capacitance spectra indicates the characteristic frequency where the capacitance plateau develops.<sup>23</sup> The inflection frequencies are found to be much lower for the devices with spiro-MeOTAD, whereas the devices without spiro-MeOTAD move their inflection points to 2–3 orders of magnitude higher frequency. This implies that the electrode polarization is much faster than the time scale for *I*–*V* hysteresis so that hysteresis-less or -free characteristics are observed for the devices without spiro-MeOTAD.

Even though it is certain that the interface of TiO<sub>2</sub>/MAPbI<sub>3</sub> and MAPbI<sub>3</sub>/spiro-MeOTAD play a critical role in development of electrode polarization, understanding of mechanism is still not fully established. The electrode polarization is basically generated by strong Coulombic interactions in the vicinity of the metal and ionic conductor interface.<sup>34</sup> Recently, experimental results reveal that MAPbI<sub>3</sub> shows both of electronic and ionic conductor characteristics,<sup>19,20,24,25</sup> which is consistent with theoretical calculations where iodide ion and iodine interstitial are suggested as a major carrier for ion migration and a prominent defect in MAPbI<sub>3</sub>, respectively.<sup>22</sup> Although there is no experimental evidence, impedance results suggest underlying chemical interaction between iodide ion and chemically reactive sites at or in selective contacts.

For the MAPbI<sub>3</sub>/spiro-MeOTAD contact, it is more complicated when considering the fact that spiro-MeOTAD layer contains additives of bis(trifluoromethane)sulfonimide lithium salt (Li-TFSI) and 4-*tert*-butylpyridine (tBP) to improve hole mobility. To elucidate the effect of additives on electrode polarization, spiro-MeOTAD layers are prepared with respect to inclusion of additives, designated as “pristine spiro-MeOTAD”, “spiro-MeOTAD + Li-TFSI”, “spiro-MeOTAD + tBP”, and “spiro-MeOTAD + Li-TFSI + tBP” in the normal structure (inset of Figure 5a). Frequency-dependent capaci-

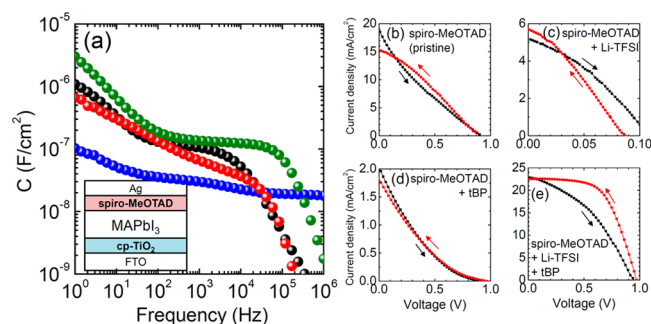


**Figure 5.** *C*–*f* curves and *I*–*V* hysteresis depending on additives in spiro-MeOTAD. (a) *C*–*f* spectra depending on additives in spiro-MeOTAD layer in dark. Black, red, blue, and green circles represent spiro-MeOTAD (pristine), spiro-MeOTAD + Li-TFSI, spiro-MeOTAD + tBP, and spiro-MeOTAD + Li-TFSI + tBP, respectively. Inset shows the device structure used for additive test. *I*–*V* hysteresis of corresponding devices including (b) pristine spiro-MeOTAD, (c) spiro-MeOTAD + Li-TFSI, (d) spiro-MeOTAD + tBP, and (e) spiro-MeOTAD + Li-TFSI + tBP. During *I*–*V* scan the current was acquired 100 ms after applying a given voltage.

tance of the four devices were measured and shown in Figure 5a. It is found that the device with pristine spiro-MeOTAD already shows considerable electrode polarization. Addition of Li-TFSI or Li-TFSI + tBP hardly declines the capacitance, but addition of tBP significantly reduces the capacitance. *I*–*V* hysteresis of devices depending on the addition of additives to

spiro-MeOTAD is well matched with a tendency of capacitance in low frequency range (Figure 5b–e), where negligible  $I-V$  hysteresis is observed for the spiro-MeOTAD + tBP case (Figure 5d). With regard to the interactions of MAPbI<sub>3</sub> with Spiro-MeOTAD, it has been widely reported that iodine and triphenylamine are easy to make a charge-transfer complex in various solution.<sup>35,36</sup> Furthermore, formation of complex is still valid with diphenylamines and their corresponding benzidines including 4-methoxytriphenylamine,<sup>35</sup> which is a major moiety of spiro-MeOTAD. We carefully suggest here that the large capacitance in low frequency range for the devices with spiro-MeOTAD might be related to underlying complexation of spiro-MeOTAD with iodide, which could develop redistribution of the localized electric field in the vicinity of MAPbI<sub>3</sub> and spiro-MeOTAD layers. Little  $I-V$  hysteresis in the presence of tBP is perhaps due to the fact that tBP seems to inhibit complexation. However, further study is needed to understand the mechanism related with additives effect in spiro-MeOTAD on  $I-V$  hysteresis.

In conclusion, we elucidated for the first time the basis for the electrode polarization of MAPbI<sub>3</sub> solar cells in low frequency range. Although the origin of  $I-V$  hysteresis is closely related to intrinsic characteristics of MAPbI<sub>3</sub>, such as ion conduction, it can be definitely suppressed by controlling interface with selective contact layers. The cp-TiO<sub>2</sub> in the normal planar structure played critical role in the electrode polarization, which is responsible for the pronounced  $I-V$  hysteresis. Moreover, the spiro-MeOTAD layer also obviously contributed to  $I-V$  hysteresis to some extent. Therefore, the replacing both cp-TiO<sub>2</sub> and spiro-MeOTAD with other selective contact layers was found to substantially reduce the capacitance along with a considerable shift of the electrode polarization domain toward higher frequency. Consequently,  $I-V$  hysteresis is eventually controllable in case that optimal selective contact layers are selected.

## ■ EXPERIMENTAL METHODS

**Synthesis of CH<sub>3</sub>NH<sub>3</sub>I.** A mixture of 28 mL of methylamine (40% in methanol, TCI) and 30 mL of hydroiodic acid (57 wt % in H<sub>2</sub>O, Aldrich) was stirred in an ice bath for 2 h. The product was obtained by evaporating the solvent at 80 °C for 2 h, washed three times with diethyl ether, and filtered. To remove the unreacted chemicals, the filtered product was recrystallized in ethanol (~150 mL) and diethyl ether (~1000 mL). The white precipitate was filtered and dried under vacuum for 12 h.

**Preparation of MAPbI<sub>3</sub> Solar Cell Devices.** ITO (Buwon, 7 Ω/sq) and FTO (Pilkington, TEC-8, 8 Ω/sq) glasses were cleaned with neutral detergent and sonicated in ethanol, acetone, and ethanol bath for 20 min, respectively. The cleaned glasses were treated with UV–ozone for 20 min.

**PEDOT:PSS/MAPbI<sub>3</sub>/PCBM Structure.** PEDOT:PSS (Clevis P VP, AI 4083, Heraeus) solution was diluted with methanol (1:1 v/v) and spin-coated at 6000 rpm (2.5 s of ramping time and 27.5 s of spin time) on cleaned ITO glass, which was heated at 150 °C for 15 min. MAPbI<sub>3</sub> was deposited by spin-coating of precursor solution using a spin-coater (WS-650-23, Laurell), where 1.7 M MAI, 1.7 M PbI<sub>2</sub>, 1.7 M *N,N*-dimethyl sulfoxide (DMSO) were dissolved together in *N,N*-dimethylformamide (99.8%, Aldrich) according to the method described elsewhere.<sup>4</sup> Diethyl ether was dropped onto the film while spinning. The spin-coated film was heated at 65 and 100 °C for 1 and 9 min, respectively. PCBM ([60]PCBM, EM

INDEX) solution (20 mg of PCBM in 1 mL of chlorobenzene) was cast on the top of the MAPbI<sub>3</sub> layer and spin-coated. Bathocuproine (BCP) (98.0%, TCI) was spin-coated on the PCBM layer using the BCP solution (0.5 mg of BCP in 1.1 mL of ethanol).

**cp-TiO<sub>2</sub>/MAPbI<sub>3</sub>/spiro-MeOTAD Structure.** cp-TiO<sub>2</sub> layer was deposited on the cleaned FTO glasses by repeating the spin-coating three times using a precursor solution containing 0.1 M titanium diisopropoxide bis(acetylacetonate) (75 wt % in 2-propanol, Aldrich) in 1-butanol (99.8%, Aldrich). Heat treatment at 125 °C for 5 min was performed between each spin-coating process and three times-coated substrate were finally heated at 500 °C for 30 min. MAPbI<sub>3</sub> was deposited in a same manner. spiro-MeOTAD solution composed of 56.4 mM 2,2',7,7'-tetrakis(*N,N*-di-*p*-methoxyphenyl-amine)-9,99-spirofluorene (spiro-MeOTAD, Merck), 29.9 mM bis-(trifluoromethane)sulfonimide lithium salt (Li-TFSI, 99.95%, Aldrich) and 188 mM 4-*tert*-butylpyridine (TBP, 96%, Aldrich) in the mixed solvent of chlorobenzene (99.8%, Aldrich) and acetonitrile (99.8%, Aldrich) (chlorobenzene:acetonitrile = 1:0.0175 v/v) was dropped on MAPbI<sub>3</sub> layer and spin-coated. PCBM/MAPbI<sub>3</sub>/spiro-MeOTAD Structure. PCBM solution (20 mg of PCBM in 1 mL of chlorobenzene) was cast on the cleaned FTO glass and spin-coated. The PCBM deposited FTO substrate was spin-coated with MAPbI<sub>3</sub> and spiro-MeOTAD in a same manner described above.

**cp-TiO<sub>2</sub>/PCBM/MAPbI<sub>3</sub>/spiro-MeOTAD Structure.** cp-TiO<sub>2</sub> layer was deposited on the cleaned FTO glasses in a same manner described in cp-TiO<sub>2</sub>/MAPbI<sub>3</sub>/spiro-MeOTAD structure. PCBM, MAPbI<sub>3</sub>, and spiro-MeOTAD layers were deposited on the prepared cp-TiO<sub>2</sub> substrate in a same manner described in PCBM/MAPbI<sub>3</sub>/spiro-MeOTAD structure.

**NiO/MAPbI<sub>3</sub>/PCBM Structure.** A solution of 60 mM nickel acetate tetrahydrate (98%, TCI) in monoethanol amine (in methoxy ethanol, 99%, Aldrich) was dropped on the cleaned FTO glass and spin-coated two times. Heat treatment at 125 °C for 5 min was carried out between spin-coating process and two times-coated substrate was finally heated at 400 °C for 30 min. MAPbI<sub>3</sub>, PCBM, and BCP layers were deposited on NiO substrate in a same manner described in PEDOT:PSS/MAPbI<sub>3</sub>/PCBM structure. For all the architectures, silver (Ag, 99.99%) was thermally deposited as a top electrode under ca. 10<sup>-6</sup> Torr.

**Current–Voltage Measurement.** Photocurrent–voltage ( $I-V$ ) curves were obtained using a solar simulator (Oriol Sol 3A class AAA) equipped with a 450 W xenon lamp (Newport 6279NS) and a Keithly 2400 source meter. One sun intensity was adjusted using a silicon solar cell (NREL-calibrated) with KG-2 filter. A metal aperture mask (0.125 cm<sup>2</sup>) was attached during the  $I-V$  curve measurement. Then, 100 ms of voltage settling time was given between applying voltage and reading current. Time-dependent transient current was measured by a Metrohm Autolab (PGSTAT 128N) under one sun illumination and recorded by a General Purpose Electrochemical System (version 4.9).

**Impedance Spectroscopy.** Impedance spectroscopic measurements were performed with PGSTAT 128N (Autolab, Eco-Chemie) by applying 20 mV of AC sinusoidal signal on the constant DC voltage from 0 to 0.6 V in dark and under one sun illumination (AM 1.5G, 100 mW/cm<sup>2</sup>). AC voltage was applied with the frequency ranging from 1 MHz to 1 Hz. The obtained Nyquist plots were fit using Z-View software where an equivalent circuit composed of a series resistance ( $R_s$ ) and

two or three R-C components (resistance and capacitance in parallel) was used.

**Morphology Investigation.** The cross-sectional scanning electron microscopy (SEM) images of perovskite solar cell were obtained from a field emission scanning electron microscope (FE-SEM, Auriga, Carl Zeiss).

## ■ ASSOCIATED CONTENT

### ■ Supporting Information

The Supporting Information is available free of charge on the ACS Publications website at DOI: 10.1021/acs.jpcllett.5b02273.

Scan rate-dependent  $I-V$  curves and their photovoltaic parameters,  $C-f$  curves depending on applied bias voltage, and cross-sectional scanning electron microscopy (SEM) images of perovskite solar cells with layout of the FTO/cp-TiO<sub>2</sub>/MAPbI<sub>3</sub>/spiro-MeOTAD/Ag, the ITO/PEDOT:PSS/MAPbI<sub>3</sub>/PCBM/BCP/Ag, the FTO/PCBM/MAPbI<sub>3</sub>/spiro-MeOTAD/Ag, the FTO/cp-TiO<sub>2</sub>/PCBM/MAPbI<sub>3</sub>/spiro-MeOTAD/Ag, and the FTO/NiO/MAPbI<sub>3</sub>/PCBM/BCP/Ag. (PDF)

## ■ AUTHOR INFORMATION

### Corresponding Author

\*E-mail: npark@skku.edu. Phone: +82-31-290-7241.

### Notes

The authors declare no competing financial interest.

## ■ ACKNOWLEDGMENTS

This work was supported by Global Frontier R&D Program on Center for Multiscale Energy System funded by the National Research Foundation under the Ministry of Science, ICT & Future Planning, Korea (under contracts No. NRF-2011-0031561, NRF-2012M3A6A7054855, and NRF-2012M3A6A7054861). H.-S.K. is grateful for the global Ph.D. fellowship grant funded by NRF (NRF-2011-0008467). A.G. and J.B. would like to thank Generalitat Valenciana (project ISIC/2012/008 Institute of Nanotechnologies for Clean Energies) and the Spanish Ministerio de Economía y Competitividad (MAT2013-47192-C3-1-R) for financial support.

## ■ REFERENCES

- (1) Kim, H.-S.; Lee, C.-R.; Im, J.-H.; Lee, K.-B.; Moehl, T.; Marchioro, A.; Moon, S.-J.; Humphry-Baker, R.; Yum, J.-H.; Moser, J. E.; et al. Lead iodide perovskite sensitized all-solid-state submicron thin film mesoscopic solar cell with efficiency exceeding 9%. *Sci. Rep.* **2012**, *2*, 591.
- (2) Kojima, A.; Teshima, K.; Shirai, Y.; Miyasaka, T. Organometal halide perovskites as visible-light sensitizers for photovoltaic cells. *J. Am. Chem. Soc.* **2009**, *131*, 6050–6051.
- (3) Im, J.-H.; Lee, C.-R.; Lee, J.-W.; Park, S.-W.; Park, N.-G. 6.5% efficient perovskite quantum-dot-sensitized solar cell. *Nanoscale* **2011**, *3*, 4088–4093.
- (4) Ahn, N.; Son, D.-Y.; Jang, I.-H.; Kang, S. M.; Choi, M.; Park, N.-G. Highly reproducible perovskite solar cells with average efficiency of 18.3% and best efficiency of 19.7% fabricated via Lewis base adduct of lead(II) iodide. *J. Am. Chem. Soc.* **2015**, *137*, 8696–8699.
- (5) Green, M. A.; Emery, K.; Hishikawa, Y.; Warta, W.; Dunlop, E. D. Solar cell efficiency tables (Version 46). *Prog. Photovoltaics* **2015**, *23*, 805–812.
- (6) Im, J.-H.; Jang, I.-H.; Pellet, N.; Grätzel, M.; Park, N.-G. Growth of CH<sub>3</sub>NH<sub>3</sub>PbI<sub>3</sub> cuboids with controlled size for high-efficiency perovskite solar cells. *Nat. Nanotechnol.* **2014**, *9*, 927–932.

- (7) Lee, J.-W.; Seol, D.-J.; Cho, A.-N.; Park, N.-G. High-efficiency perovskite solar cells based on the black polymorph of HC-(NH<sub>2</sub>)<sub>2</sub>PbI<sub>3</sub>. *Adv. Mater.* **2014**, *26*, 4991–4998.

- (8) Nie, W.; Tsai, H.; Asadpour, R.; Blancon, J.-C.; Neukirch, A. J.; Gupta, G.; Crochet, J. J.; Chhowalla, M.; Tretiak, S.; Alam, M. A.; et al. High-efficiency solution-processed perovskite solar cells with millimeter-scale grains. *Science* **2015**, *347*, 522–525.

- (9) Jeon, N. J.; Noh, J. H.; Yang, W. S.; Kim, Y. C.; Ryu, S.; Seo, J.; Seok, S. I. Compositional engineering of perovskite materials for high-performance solar cells. *Nature* **2015**, *517*, 476–480.

- (10) Stranks, S. D.; Eperon, G. E.; Grancini, G.; Menelaou, C.; Alcocer, M. J. P.; Leijtens, T.; Herz, L. M.; Petrozza, A.; Snaith, H. J. Electron-hole diffusion lengths exceeding 1 micrometer in an organometal trihalide perovskite absorber. *Science* **2013**, *342*, 341–344.

- (11) Kim, H.-S.; Mora-Sero, I.; Gonzalez-Pedro, V.; Fabregat-Santiago, F.; Juarez-Perez, E. J.; Park, N.-G.; Bisquert, J. Mechanism of carrier accumulation in perovskite thin-absorber solar cells. *Nat. Commun.* **2013**, *4*, 2242.

- (12) Gonzalez-Pedro, V.; Juarez-Perez, E. J.; Arsyad, W.-S.; Barea, E. M.; Fabregat-Santiago, F.; Mora-Sero, I.; Bisquert, J. General Working principles of CH<sub>3</sub>NH<sub>3</sub>PbX<sub>3</sub> perovskite solar cells. *Nano Lett.* **2014**, *14*, 888–893.

- (13) Edri, E.; Kirmayer, S.; Mukhopadhyay, S.; Gartsman, K.; Hodes, G.; Cahen, D. Elucidating the charge carrier separation and working mechanism of CH<sub>3</sub>NH<sub>3</sub>PbI<sub>3-x</sub>Cl<sub>x</sub> perovskite solar cells. *Nat. Commun.* **2014**, *5*, 3461.

- (14) Juarez-Perez, E. J.; Sanchez, R. S.; Badia, L.; Garcia-Belmonte, G.; Kang, Y. S.; Mora-Sero, I.; Bisquert, J. Photoinduced giant dielectric constant in lead halide perovskite solar cells. *J. Phys. Chem. Lett.* **2014**, *5*, 2390–2394.

- (15) Yin, W.-J.; Shi, T.; Yan, Y. Unique properties of halide perovskites as possible origins of the superior solar cell performance. *Adv. Mater.* **2014**, *26*, 4653–4658.

- (16) Kim, H.-S.; Kim, S. K.; Kim, B. J.; Shin, K.-S.; Gupta, M. K.; Jung, H. S.; Kim, S.-W.; Park, N.-G. Ferroelectric polarization in CH<sub>3</sub>NH<sub>3</sub>PbI<sub>3</sub> perovskite. *J. Phys. Chem. Lett.* **2015**, *6*, 1729–1735.

- (17) Xiao, Z.; Yuan, Y.; Shao, Y.; Wang, Q.; Dong, Q.; Bi, C.; Sharma, P.; Gruverman, A.; Huang, J. Giant switchable photovoltaic effect in organometal trihalide perovskite devices. *Nat. Mater.* **2014**, *14*, 193–198.

- (18) Kim, H.-S.; Park, N.-G. Parameters affecting I-V hysteresis of CH<sub>3</sub>NH<sub>3</sub>PbI<sub>3</sub> perovskite solar cells: effects of perovskite crystal size and mesoporous TiO<sub>2</sub> layer. *J. Phys. Chem. Lett.* **2014**, *5*, 2927–2934.

- (19) Tress, W.; Marinova, N.; Moehl, T.; Zakeeruddin, S. M.; Nazeeruddin, M. K.; Grätzel, M. Understanding the rate-dependent J-V hysteresis, slow time component, and aging in CH<sub>3</sub>NH<sub>3</sub>PbI<sub>3</sub> perovskite solar cells: the role of a compensated electric field. *Energy Environ. Sci.* **2015**, *8*, 995–21004.

- (20) Unger, E. L.; Hoke, E. T.; Bailie, C. D.; Nguyen, W. H.; Bowring, A. R.; Heumüller, T.; Christoforo, M. G.; McGehee, M. D. Hysteresis and transient behavior in current-voltage measurements of hybrid-perovskite absorber solar cells. *Energy Environ. Sci.* **2014**, *7*, 3690–3698.

- (21) Yuan, Y.; Chae, J.; Shao, Y.; Wang, Q.; Xiao, Z.; Centrone, A.; Huang, J. Photovoltaic switching mechanism in lateral structure hybrid perovskite solar cells. *Adv. Energy Mater.* **2015**, *5*, 1500615.

- (22) Du, H. M. Efficient carrier transport in halide perovskites: theoretical perspectives. *J. Mater. Chem. A* **2014**, *2*, 9091–9098.

- (23) Duan, H.-S.; Zhou, H.; Chen, Q.; Sun, P.; Luo, S.; Song, T.-B.; Bob, B.; Yang, Y. The identification and characterization of defect states in hybrid organic-inorganic perovskite photovoltaics. *Phys. Chem. Chem. Phys.* **2015**, *17*, 112–116.

- (24) Zhang, Y.; Liu, M.; Eperon, G. E.; Leijtens, T. C.; McMeekin, D.; Saliba, M.; Zhang, W.; de Bastiani, M.; Petrozza, A.; Herz, L. M.; et al. Charge selective contacts, mobile ions and anomalous hysteresis in organic-inorganic perovskite solar cells. *Mater. Horiz.* **2015**, *2*, 315–322.

(25) Almora, O.; Zarazua, I.; Mas-Marza, E.; Mora-Sero, I.; Bisquert, J.; Garcia-Belmonte, G. Capacitive dark currents, hysteresis, and electrode polarization in lead halide perovskite solar cells. *J. Phys. Chem. Lett.* **2015**, *6*, 1645–1652.

(26) Heo, J. H.; Han, H. J.; Kim, D.; Ahn, T. K.; Im, S. H. Hysteresis-less inverted  $\text{CH}_3\text{NH}_3\text{PbI}_3$  planar perovskite hybrid solar cells with 18.1% power conversion efficiency. *Energy Environ. Sci.* **2015**, *8*, 1602–1608.

(27) Forgács, D.; Sessolo, M.; Bolink, H. J. Lead acetate precursor based p-i-n perovskite solar cells with enhanced reproducibility and low hysteresis. *J. Mater. Chem. A* **2015**, *3*, 14121–14125.

(28) Jeon, N. J.; Noh, J. H.; Kim, Y. C.; Yang, W. S.; Ryu, S.; Seok, S. I. Solvent engineering for high-performance inorganic-organic hybrid perovskite solar cells. *Nat. Mater.* **2014**, *13*, 897–903.

(29) Heo, J. H.; Song, D. H.; Han, H. J.; Kim, S. Y.; Kim, J. H.; Kim, D.; Shin, H. W.; Ahn, T. K.; Wolf, C.; Lee, T.-W.; et al. Planar  $\text{CH}_3\text{NH}_3\text{PbI}_3$  perovskite solar cells with constant 17.2% average power conversion efficiency irrespective of the scan rate. *Adv. Mater.* **2015**, *27*, 3424–3430.

(30) Dualah, A.; Moehl, T.; Tétreault, N.; Teuscher, J.; Gao, P.; Nazeeruddin, M. K.; Grätzel, M. Impedance spectroscopic analysis of lead iodide perovskite-sensitized solid-state solar cells. *ACS Nano* **2014**, *8*, 362–373.

(31) Tao, C.; Neutzner, S.; Colella, L.; Marras, S.; Kandada, A. R. S.; Gandini, M.; Bastiani, M. D.; Pace, G.; Manna, L.; Caironi, M.; et al. 17.6% steady state efficiency in low-temperature processed standard-architecture planar solar cells with the perovskite absorber grown onto a PCBM-based electron extraction layer. *Energy Environ. Sci.* **2015**, *8*, 2365–2370.

(32) Wang, Q.; Shao, Y.; Dong, Q.; Xiao, Z.; Yuan, Y.; Huang, J. Large fill-factor bilayer iodine perovskite solar cells fabricated by a low-temperature solution-process. *Energy Environ. Sci.* **2014**, *7*, 2359–2365.

(33) Wojciechowski, K.; Stranks, S. D.; Abate, A.; Sadoughi, G.; Sadhanala, A.; Kopidakis, N.; Rumbles, G.; Li, C.-Z.; Friend, R. H.; Jen, A. K.-Y.; et al. Heterojunction modification for highly efficient organic-inorganic perovskite solar cells. *ACS Nano* **2014**, *8*, 12701–12709.

(34) Serghai, A.; Tress, M.; Sangoro, J. R.; Kremer, F. Electrode polarization and charge transport at solid interfaces. *Phys. Rev. B: Condens. Matter Mater. Phys.* **2009**, *80*, 184301.

(35) Bruning, W. H.; Nelson, R. F.; Marcoux, L. S.; Adams, R. N. The structure of the iodine-triphenylamine charge-transfer complex. *J. Phys. Chem.* **1967**, *71*, 3055–3057.

(36) Niu, H.; Cai, J.; Zhao, P.; Wang, C.; Bai, X.; Wang, W. Simple approach to regulate the spectra of novel kinds of polyazomethines containing bulky triphenylamine: electrochemistry, electrochromism and photophysical responsive to environment. *Dyes Pigm.* **2013**, *96*, 158–169.